




Communication

Chemical Transformation Induced Core–Shell Ni₂P@Fe₂P Heterostructures toward Efficient Electrocatalytic Oxygen Evolution

Huijun Song ^{1,†}, Jingjing Li ^{1,†}, Guan Sheng ^{2,†}, Ruilian Yin ¹, Yanghang Fang ¹, Shigui Zhong ¹, Juan Luo ¹, Zhi Wang ¹, Ahmad Azmin Mohamad ²  and Wei Shao ^{1,*}

¹ State Key Laboratory Breeding Base of Green Chemistry Synthesis Technology, College of Chemical Engineering, Zhejiang University of Technology, Hangzhou 310014, China

² School of Materials and Mineral Resources Engineering, University Sains Malaysia, Nibong Tebal 14300, Malaysia

* Correspondence: weishao@zjut.edu.cn

† These authors have contributed equally to this work.

Abstract: The oxygen evolution reaction (OER) is a crucial reaction in water splitting, metal–air batteries, and other electrochemical conversion technologies. Rationally designed catalysts with rich active sites and high intrinsic activity have been considered as a hopeful strategy to address the sluggish kinetics for OER. However, constructing such active sites in non-noble catalysts still faces grand challenges. To this end, we fabricate a Ni₂P@Fe₂P core–shell structure with outperforming performance toward OER via chemical transformation of rationally designed Ni-MOF hybrid nanosheets. Specifically, the Ni-MOF nanosheets and their supported Fe-based nanomaterials were in situ transformed into porous Ni₂P@Fe₂P core–shell nanosheets composed of Ni₂P and Fe₂P nanodomains in homogenous dispersion via a phosphorization process. When employed as the OER electrocatalyst, the Ni₂P@Fe₂P core–shell nanosheets exhibits excellent OER performance, with a low overpotential of 238/247 mV to drive 50/100 mA cm^{−2}, a small Tafel slope of 32.91 mV dec^{−1}, as well as outstanding durability, which could be mainly ascribed to the strong electronic interaction between Ni₂P and Fe₂P nanodomains stabilizing more Ni and Fe atoms with higher valence. These high-valence metal sites promote the generation of high-active Ni/FeOOH to enhance OER activity.

Keywords: Ni₂P@Fe₂P; heterostructures; oxygen evolution reaction



Citation: Song, H.; Li, J.; Sheng, G.; Yin, R.; Fang, Y.; Zhong, S.; Luo, J.; Wang, Z.; Mohamad, A.A.; Shao, W. Chemical Transformation Induced Core–Shell Ni₂P@Fe₂P Heterostructures toward Efficient Electrocatalytic Oxygen Evolution. *Nanomaterials* **2022**, *12*, 3153. <https://doi.org/10.3390/nano12183153>

Academic Editor: João Pedro Araújo

Received: 22 August 2022

Accepted: 7 September 2022

Published: 11 September 2022

Publisher's Note: MDPI stays neutral with regard to jurisdictional claims in published maps and institutional affiliations.



Copyright: © 2022 by the authors. Licensee MDPI, Basel, Switzerland. This article is an open access article distributed under the terms and conditions of the Creative Commons Attribution (CC BY) license (<https://creativecommons.org/licenses/by/4.0/>).

1. Introduction

Developing sustainable and clean energy is crucial for satisfying the ever-increasing energy demand and existing environmental problems [1–3]. However, the intermittency in generated energy sources, primarily through solar and wind, impedes the storage of produced energy, owing to limited grid-scale battery capacity. Electrochemical water splitting has great potential to utilize such intermittent energy to generate clean hydrogen sources. However, the hydrogen evolution reaction at the cathode is seriously limited by the sluggish kinetics in the OER (oxygen evolution reaction) at the anode. Thus, it is urgent to explore active electrocatalysts with high oxygen evolution reaction (OER) performance to achieve the industrial utility of water splitting for hydrogen production.

Until now, considerable efforts have been made to explore Earth-abundant and high-efficiency transition metal-based OER catalysts, including layered double hydroxides (LDHs) [4], metal oxides [5], phosphides [6], selenides [7], sulfides [8], nitrides [9], and so on. Among them, transition-metal phosphides (TMPs) have been considered as promising candidates for alkaline OER catalysis because of their good electrical conductivity with metalloid characteristics and remarkable durability in working conditions with strong alkaline electrolytes and theoretically outstanding electrochemical catalytic behaviors [10–14].

During the alkaline OER, the metal-p bond could promote the formation of metal oxyhydroxides with rich defects and low-crystalline properties. The TMPs could be transformed into TMPs/MO_x with a unique core-shell structure. The TMP core as conductive support could facilitate the rapid and effective electron transfer process and synergistically enhance the MO_x shell as species demonstrating higher electrochemical performance [15,16]. Although these TMP-based electrocatalysts have been proved to have great potential for the OER, their activities are still not enough to achieve the requirements of industrial applications with large current density ($\geq 500 \text{ mA cm}^{-2}$) at low overpotentials ($< 300 \text{ mV}$) [17]. For further improvement in the catalytic behaviors of TMP-based catalysis, heterostructure engineering has been considered as an effective strategy and widely carried out. The heterostructure can be extensively fabricated through the hybridization of various transition-metal electrocatalysts. It can merge the structural advantages of each component and generate abundant active sites and electronic reconfigured interfaces, which collectively accelerate the reaction kinetics and, thus, modify the catalytic performance of nanocomposites [18–20]. For example, Huang regulated the electronic configuration of Ni and N atoms around the Fermi level to boost overall water splitting by constructing the heterointerface of Ni₃N@2M-MoS₂ [21]. Du modulated the local structures and electronic environments via constructing Cu@CeO₂ nanotube with the deposition of NiFeCr hydroxide, leading to catalysts with sufficient active sites, quick oxygen diffusion, and releasement; the d-f orbital coupling for great promoted electron transfer and, therefore, demonstrating enhanced OER performance [22]. However, constructing catalytically active heterostructures with novel composition and architecture still remains poorly developed due to the synthetic challenge.

Considering the above discussion, herein, a simple strategy was proposed to prepare Ni₂P@Fe₂P core-shell nanosheets as high active catalysts for OER by the chemical transformation of rationally fabricated Ni-MOF hybrid nanosheets. The obtained Ni₂P@Fe₂P 2D hieratic structure was composed of homogeneous dispersion of Fe₂P and Ni₂P nanodomains, which induces the synergistic effect of different components, affording the Ni₂P@Fe₂P nanosheets with more stabilized high-valence metal active sites to promote the generation of high-active Ni/FeOOH during the OER process and result in outperforming OER performance. As expected, the designed Ni₂P@Fe₂P nanosheets demonstrate ultralow overpotentials of 210/247 mV at 10/100 mA cm⁻² and afford more than 36 h durability with negligible decay in OER under multi-current densities.

2. Materials and Methods

The experimental details, including the Materials and Methods, are listed in the Supplementary Materials.

3. Results and Discussion

Figure 1a schematically illustrates the fabrication of NF-supported hierarchical 2D core-shell Ni₂P@Fe₂P nanosheets. First, the novel 2D Ni-MOF nanosheets were synthesized on NF using DMAP as organic ligands coordinated with nickel salts. Subsequently, the as-prepared Ni-MOF nanoarray was soaked in FeCl₂·4H₂O ethanol solution at 90 °C for 15 h and the Ni-MOF uniformly covered with Fe-based nanoparticles on the surface was obtained, followed by the phosphorization treatment with NaH₂PO₄·2H₂O as a phosphorus source to prepare the hierarchical 2D core-shell Ni₂P@Fe₂P nanosheets. As shown in Figure 1b–d, in situ grown self-supported Ni-MOF nanosheets are highly dispersive and vertically stacked on the Ni foam. In addition, the lateral size and thickness of the nanosheets are several hundred nanometers and about 25 nm, respectively. After soaking treatment in the FeCl₂·4H₂O ethanol solution, the surface of obtained Ni-MOF@Fenano nanosheets was covered with some tiny nanoparticles (Figure 1e,f). In addition, the thickness of the nanosheets increased to 40 nm. The corresponding energy-dispersive X-ray spectroscopy (EDS) mapping images (Figure S1) indicate that the Ni and Fe elements are mainly dispersed in the inner nanosheets and out of tiny nanoparticles, suggesting Ni-MOF@Fenano with a core-shell structure. The EDS spectrum (Figure S2) reveals that

the ratio of Fe/Ni is about 0.096. After chemical transformation by thermal phosphorization at 300 °C for 2 h with $\text{NaH}_2\text{PO}_4 \cdot 2\text{H}_2\text{O}$, it is obvious that the obtained $\text{Ni}_2\text{P}@Fe_2\text{P}$ basically inherited the overall morphology of Fe-based nanoparticle-decorated Ni-MOF nanosheets. The pure Ni_2P nanosheets and Fe_2P supported on the NF were also fabricated as reference. Figure 1e–g demonstrate that the Ni-MOF-derived Ni_2P nanosheets were vertically stacked on the NF and plenty of large holes could be obviously found in Ni_2P nanosheets (Figure S3), while the synthesized Fe_2P exhibited irregular nano bulks (Figure S4). Therefore, we can infer that during the thermal phosphorization of the Ni-MOF@Fenano materials, the Fenano shell and Ni-MOF core were etched by PH_3 and then transformed into core-shell structured $\text{Ni}_2\text{P}@Fe_2\text{P}$ nanosheets and the Fe_2P shell can act as a protecting layer, preventing the structure collapse of Ni_2P nanosheets.

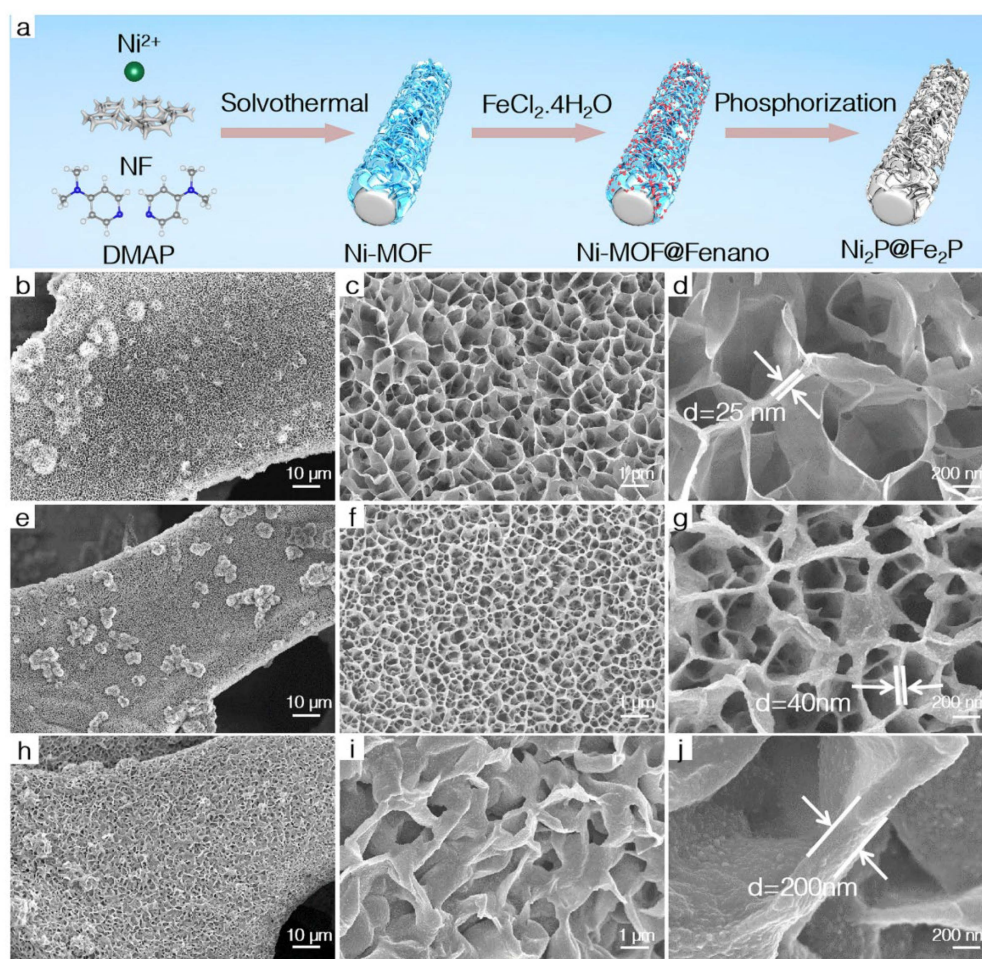


Figure 1. (a) Schematic illustration for the synthesis of the $\text{Ni}_2\text{P}@Fe_2\text{P}$. SEM images of Ni-MOF (b–d), Ni-MOF@Fenano (e–g) and $\text{Ni}_2\text{P}@Fe_2\text{P}$ (h–j).

High-angle annular dark-field scanning transmission electron microscopy (HAADF-STEM) was used to detect the element composition and dispersion in the $\text{Ni}_2\text{P}@Fe_2\text{P}$. The HAADF image in Figure S5 shows that the core-shell $\text{Ni}_2\text{P}@Fe_2\text{P}$ nanosheets are composed of tiny nanoparticles. The EDS mapping images (Figures 2a and S5) of the $\text{Ni}_2\text{P}@Fe_2\text{P}$ clearly state that the Ni and Fe elements are mainly distributed in the core and shell of $\text{Ni}_2\text{P}@Fe_2\text{P}$, respectively, while the P elements are homogeneously distributed over the entire $\text{Ni}_2\text{P}@Fe_2\text{P}$. A similar ratio of Fe/Ni to that for Ni-MOF@Fenano was determined by the EDS spectrum (Figure S6). XRD test was firstly carried out to determine the crystal phases of as-prepared $\text{Ni}_2\text{P}@Fe_2\text{P}$, Fe_2P , and Ni_2P . As shown in Figure 3a, all the diffraction peaks of the $\text{Ni}_2\text{P}@Fe_2\text{P}$ match well with Fe_2P (JCPDS No. 01-078-6794) or Ni_2P (JCPDS No. 01-072-2514), suggesting a similar crystal structure of Fe_2P and Ni_2P nanodomains

in $\text{Ni}_2\text{P@Fe}_2\text{P}$ nanosheets. In addition, the Fe_2P demonstrates similar diffraction peaks with that of $\text{Ni}_2\text{P@Fe}_2\text{P}$, while two additional peaks (located at 38.5° and 49.1°) indexed to Ni_{12}P_5 (JCPDS No. 22-1190) could be found in as-prepared Ni_2P samples (Figure S8). The HRTEM was further conducted for the atomic-scale structural identification of $\text{Ni}_2\text{P@Fe}_2\text{P}$ nanosheets. Figure 2b shows a HRTEM image of $\text{Ni}_2\text{P@Fe}_2\text{P}$ nanosheets. The selected area (marked with a red rectangle in Figure 2b) HRTEM image (Figure 2c) and its denoised image (Figure 2d) unravel the $\{010\}$ planes where the lattice spacing is 5.0 \AA , affirming its identity from crystallography since it matches well with the crystalline model of Ni_2P (or Fe_2P , because of their same crystal structure) observed along the $[001]$ axis (Figure 2f) and the corresponding projected potential (Figure 2g). The corresponding Fast Fourier transform pattern (Figure 2e) in Figure 2d also fits well with the simulated corresponding FFT (Figure 2h). In conclusion, the HRTEM results reveal that the $\text{Ni}_2\text{P@Fe}_2\text{P}$ 2D hieratic structure is composed of homogeneous dispersion of Fe_2P and Ni_2P nanodomains.

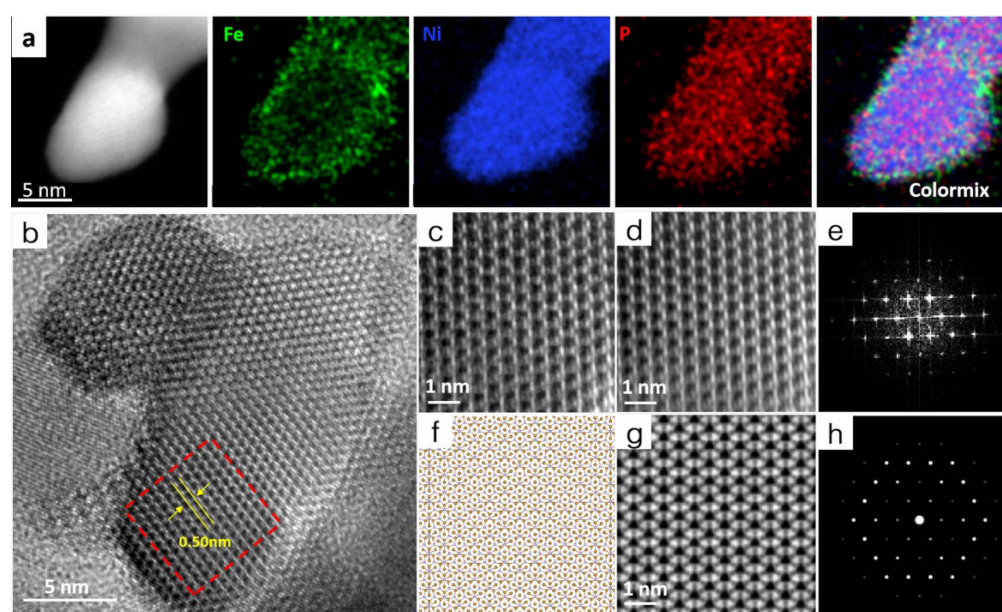


Figure 2. (a) HAADF-STEM and the corresponding EDS mapping images of $\text{Ni}_2\text{P@Fe}_2\text{P}$. (b) High-magnification TEM image of $\text{Ni}_2\text{P@Fe}_2\text{P}$ heterostructure. (c) Select-area HRTEM view of the crystalline region of Ni_2P . (d) Denoised image of Figure 2c. (f) The crystal structure model of Ni_2P observed along the $[001]$ axis. (g) The projected potential of Ni_2P observing along the $[001]$ axis. (e) FFT of Figure 2d and (h) simulated FFT of the crystal structure model of Ni_2P observed along the $[001]$ axis.

Heterostructure engineering has been reported to be an effective strategy to modulate the electronic structure of active sites and, therefore, effectively adjusts the catalytic behaviors of the catalysts [18,23,24]. Hence, an X-ray photoelectron spectroscopy (XPS) test was conducted to investigate the surface electronic configuration and chemical composition of prepared samples. The survey spectra (Figure S7) confirm the coexistence of Ni, Fe, P, and O elements in $\text{Ni}_2\text{P@Fe}_2\text{P}$ and Fe_2P samples, while the prepared Ni_2P is mainly composed of Ni, P, and O elements, which suggests the successful decoration of Fe-based nanomaterials on the Ni-MOF nanosheets. The Ni element in Fe_2P samples may be ascribed to the generation of Ni_2P resulting from the corrosion of Ni foam by PH_3 . The existence of O could originate from the surface oxidation of samples in the air or unavoidable adsorbed oxygen species. In the high-resolution P 2p spectra, the Fe_2P and $\text{Ni}_2\text{P@Fe}_2\text{P}$ exhibit lower binding energy than that of Ni_2P (Figure 3b). In the high-resolution Ni 2p spectra of all samples (Figure 3c), two peaks located at about 856 eV and 874 eV with satellite peaks can be attributed to the $\text{Ni}^{2+} 2p_{3/2}$ and $\text{Ni}^{2+} 2p_{1/2}$ of Ni^{2+} in surface oxide [25]. In addition, a single peak of about 853 eV could be assigned to Ni-P species [26]. The binding energy

of Ni-P is lower than that of Ni-O due to the weaker electronegativity of P, which means difficulty for electrons to dissociate from the metal ion. It is noted that the peaks for Ni-O and Ni-P species of $\text{Ni}_2\text{P@Fe}_2\text{P}$ and Fe_2P exhibit large and small positive shifts, respectively, compared with those observed from the Ni_2P spectrum. A similar positive shift in the peaks for Fe-O and Fe-P species of $\text{Ni}_2\text{P@Fe}_2\text{P}$ is evident compared with those observed from the Fe_2P spectrum (Figure 3d). Such positive shifts indicate the generation of more Ni and Fe atoms with higher valence, which imply the strong electronic interaction between Ni_2P and Fe_2P in $\text{Ni}_2\text{P@Fe}_2\text{P}$ nanosheets. In addition, stabilized metals with higher valence have been widely considered with outperforming performance for OER, because they could enhance the chemisorption of OH^- and promote the in situ generation of MOOH as high-active sites (M represents metal) through nucleophilic attack during OER [27,28]. Therefore, the as-synthesized biphasic $\text{Ni}_2\text{P@Fe}_2\text{P}$ nanosheets demonstrate great potential to evoke synergistic electrocatalysis for OER.

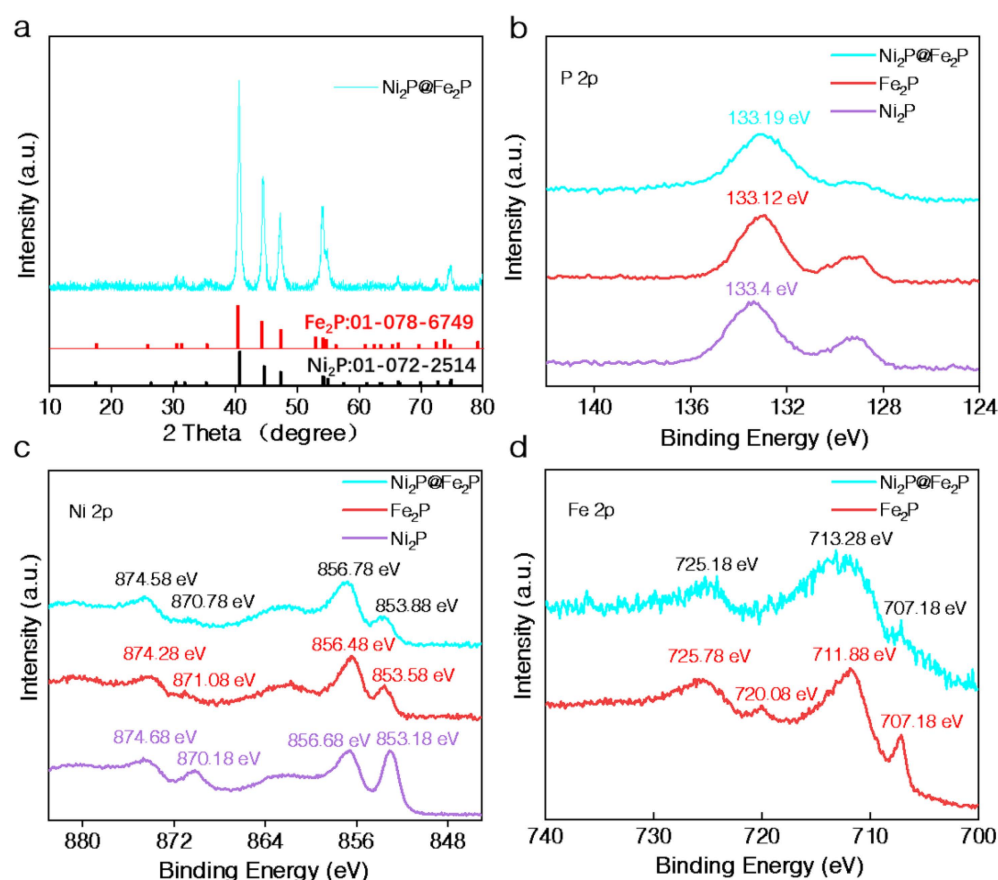


Figure 3. (a) XRD pattern of $\text{Ni}_2\text{P@Fe}_2\text{P}$. (b) High-resolution P 2p XPS spectra of the $\text{Ni}_2\text{P@Fe}_2\text{P}$, Fe_2P and Ni_2P . (c) High-resolution Ni 2p XPS spectra of the $\text{Ni}_2\text{P@Fe}_2\text{P}$, Fe_2P and Ni_2P . (d) High-resolution Fe 2p XPS spectra of the $\text{Ni}_2\text{P@Fe}_2\text{P}$ and Fe_2P .

The OER performance was evaluated using a three-electrode system in 1 M KOH. The NF supported NiFe-LDH commercial RuO_2 and IrO_2 deposited on the NF were also assessed as references. SEM images in Figure S9 show that the prepared NiFe-LDH is composed of plenty of nanowires and nanosheets. Figures 4a and S10 display the polarization curves (corrected with iR losses) for all samples. The $\text{Ni}_2\text{P@Fe}_2\text{P}$ catalyst demonstrates the highest activity, requires a small overpotential (η) of 210 mV to achieve a current density of 10 mA cm^{-2} , outperforming Fe_2P (238 mV), Ni_2P (262 mV), NiFe-LDH (223 mV), RuO_2 (292 mV), IrO_2 (337 mV), and pure NF (390 mV) (Figure 4b). Furthermore, the $\text{Ni}_2\text{P@Fe}_2\text{P}$ can reach a large current density of 50 and 100 mA cm^{-2} at the overpotential of 238/247 mV, which is comparable with the most reported active transition-metal-based

OER electrocatalysts (Table S1) [28–43]. Of note, the peaks around 1.36–1.41 V (vs. RHE) in Figure 4a are corresponding with the oxidation of Ni species [44,45]. Among them, the redox peak of Ni₂P@Fe₂P nanosheets shows a positive shift compared with that of Ni₂P nanosheets, suggesting the formation of Ni⁴⁺ of Ni₂P@Fe₂P during OER, which has the modulated d-band center and reduced the adsorption energy of oxygenated intermediates on the surface of the catalyst. In addition, the increased Ni⁴⁺ content will lead to greater Ni-O covalency during OER and, thus, greater oxyl character, which could directly correlate with enhanced activity of the catalyst in promoting OER [46,47]. The corresponding Tafel plots (Figure 4c) show a decreasing trend in Tafel slope from Ni₂P (64.56 mV dec^{−1}), NiFe-LDH (52.97 mV dec^{−1}), Fe₂P (40.58 mV dec^{−1}) to Fe₂P@Ni₂P (32.91 mV dec^{−1}), demonstrating the faster OER kinetics for the Fe₂P@Ni₂P electrode, which may be ascribed to the modulated electronic structure of metal active sites according to the LSV and XPS results. To gain further insights into the superior OER activity of Fe₂P@Ni₂P electrode catalysts, cyclic voltammetry (CV) curves with different scan rates were collected to analyze electrochemically double-layer capacitance (C_{dl}), which is proportional to electrochemically active surface area (ECSA) (Figure S11). As displayed in Figure 4d, the Ni₂P nanosheets have the highest value of C_{dl} of 6.11 mF cm^{−2}, which is larger than that of Ni₂P@Fe₂P (5.56 mF cm^{−2}) and Fe₂P (4.66 mF cm^{−2}), indicating that the Ni₂P nanosheets enhance more accessible active sites in the core-shell Ni₂P@Fe₂P for the OER. Notably, the lowest OER activity of Ni₂P indicates that the intrinsic activity rather than the ECSA of the samples is the key to OER activity. Furthermore, the chronopotentiometry experiments without iR compensation were conducted to explore the durability. Figure 4e presents the chronopotentiometry response of Ni₂P@Fe₂P at multicurrent densities. A negligible activity degradation is observed for Ni₂P@Fe₂P after a 36 h test. In addition, the stability test of IrO₂ at 10 mA cm^{−2} demonstrates obvious activity degradation after a 5 h test (Figure S12a). This suggests the superb durability of the core-shell Ni₂P@Fe₂P for OER. The EIS characterizations were also tested and the Nyquist plot (Figure S12b) demonstrates that the Ni₂P@Fe₂P has the smallest Rct, suggesting its faster electron transport during OER, thus, promising a higher OER activity.

Previous reports have demonstrated that many transition-metal-based OER catalysts undergo substantial reconstruction to form mixed-metal oxyhydroxides [48–50]. Hence, the structure information of the catalysts after the LSV test was investigated to identify the intrinsic origins of the excellent OER performance. SEM and TEM images (Figure S13) show that the morphology of Ni₂P@Fe₂P demonstrated obvious changes; plenty of newly formed small nanosheets on the surface of Ni₂P@Fe₂P nanosheets were observed. The corresponding HAADF STEM mapping (Figure S14) revealed that the newly formed small nanosheets are mainly composed of Fe, Ni, and O elements, while the inner nanosheets are mainly composed of Fe, Ni, and P elements, indicating significant surface structure conversion of Ni₂P@Fe₂P nanosheets during the OER process. In addition, a newly formed Raman band (Figure S15) located at about 558 cm^{−1} was observed for Ni₂P@Fe₂P and this new band is likely to be ascribed to Fe/Ni-O vibrations in NiFeOOH [26,49]. Therefore, we can infer that the surface of Ni₂P@Fe₂P was partially transformed into NiFeOOH nanosheets during the OER process and resulted in hierarchically core-shell structured nanosheets. The XPS spectra of Ni₂P@Fe₂P after the LSV test were also conducted to investigate the evolution of elemental composition and valence. The disappearance of characteristic peaks for metal-p bond in the Ni and Fe fine spectra further demonstrate the surface transformation of Ni₂P@Fe₂P during the OER process and the positive shift in the binding energy for Fe-O and Ni-O species may be ascribed to the formed NiFeOOH on the surface of Ni₂P@Fe₂P (Figure S16). Therefore, we can infer that the interactions between Ni₂P and Fe₂P in catalysts promote its surface transformation during the OER process and the in situ formatted metal oxyhydroxides from the TM-based electrocatalysts usually are considered with high activity toward OER.

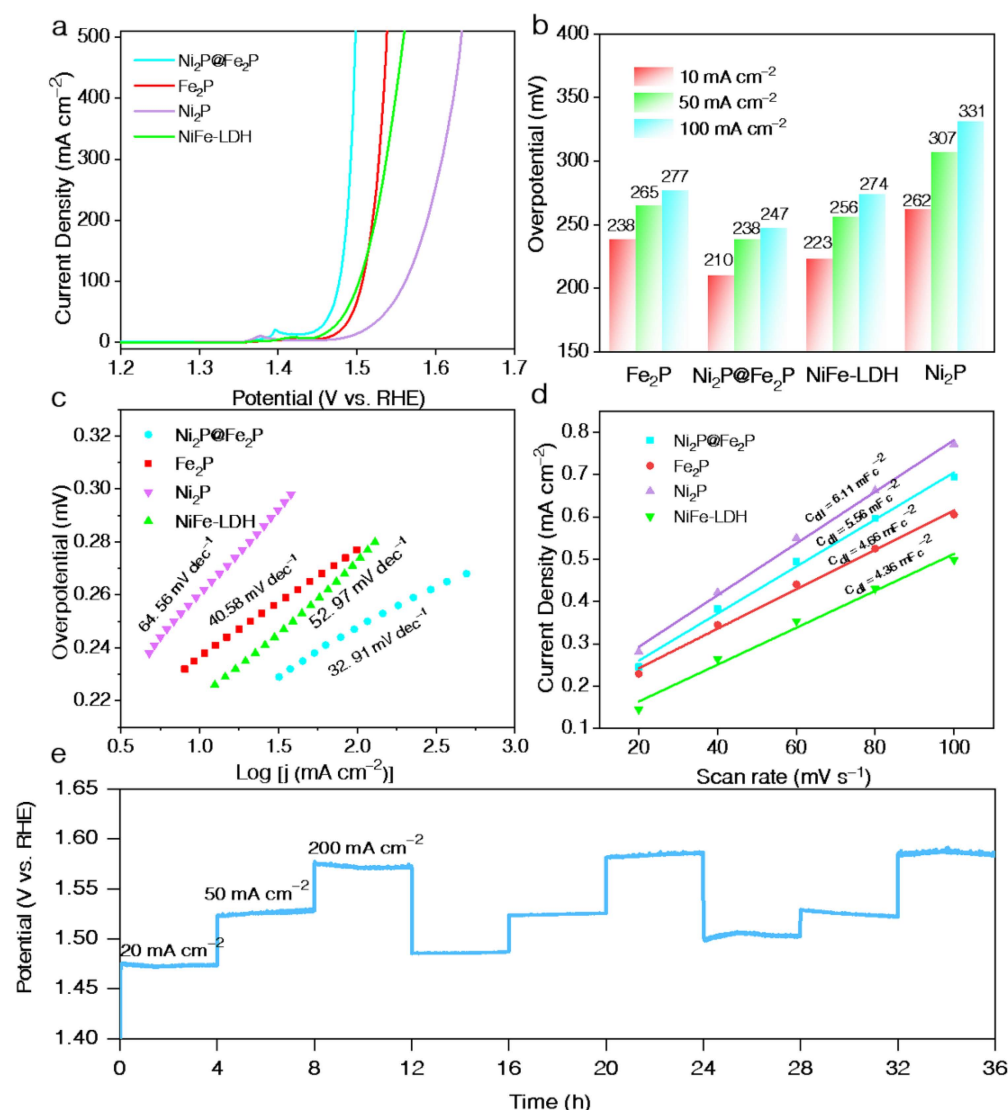


Figure 4. (a) LSV curves of Fe₂P, Ni₂P@Fe₂P, NiFe-LDH and Ni₂P. (b) Comparison of the overpotentials at 10 mA cm⁻², 50 mA cm⁻² and 100 mA cm⁻² for Fe₂P, Ni₂P@Fe₂P, NiFe-LDH and Ni₂P. (c) Tafel curves of Fe₂P, Ni₂P@Fe₂P, NiFe-LDH and Ni₂P. (d) C_{dl} values of Ni₂P, NiFe-LDH, Ni₂P@Fe₂P and Fe₂P. (e) Durability test of Ni₂P@Fe₂P at constant 20 mA cm⁻², 50 mA cm⁻² and 200 mA cm⁻².

4. Conclusions

In summary, a well-defined Ni₂P@Fe₂P nanosheet structure as an excellent electrocatalyst for OER was successfully built through the chemical transformation of Ni-MOF hybrid nanosheets. Benefiting from their heterostructure nanosheet affording the synergetic effect of the two components, the reduced overpotential was achieved through stabilized high-valence metal sites promoting the formation of Ni/FeOOH. The resultant Ni₂P@Fe₂P nanosheets electrocatalyst exhibits outperforming OER performance with a low overpotential of 210 mV at 10 mA cm⁻², a Tafel slope of 32.91 mV dec⁻¹, and excellent durability in 36 h of OER test.

Supplementary Materials: The following supporting information can be downloaded at: <https://www.mdpi.com/article/10.3390/nano12183153/s1>, Figure S1: HAADF STEM and corresponding EDS mapping images of Ni-MOF@Fenano. Figure S2: EDS spectrum of Fenano. Figure S3: (a,b) SEM images of Ni₂P. Figure S4: SEM images of Fenano (a,b) and Fe₂P (c,d). Figure S5: HAADF STEM and corresponding EDS mapping images of Ni₂P@Fe₂P. Figure S6: EDS spectrum of as-prepared

Ni₂P@Fe₂P. Figure S7: XPS survey spectra of the Ni₂P, Ni₂P@Fe₂P and Fe₂P. Figure S8: XRD patterns of (a) Fe₂P and (b) Ni₂P. Figure S9: (a–c) SEM images of LDH with different magnifications. Figure S10: LSV curves of IrO₂, RuO₂ and Ni foam. Figure S11: CV curves of (a) Fe₂P, (b) NiFe-LDH, (c) Ni₂P@Fe₂P, and (d) Ni₂P acquired at various scan rates. Figure S12: Durability test of Ir₂O₃@10 mA cm^{−2}. (b) Nyquist plots. Figure S13: (a,b) SEM images of Ni₂P@Fe₂P after LSV test. (c) TEM image of Ni₂P@Fe₂P. (d) TEM image of Ni₂P@Fe₂P after LSV test. Figure S14: HAADF STEM and corresponding EDS mapping images of Ni₂P@Fe₂P after LSV test. Figure S15: Raman spectra of Ni₂P@Fe₂P before and after LSV test. Figure S16: High-resolution XPS spectra of (a) Ni 2p, (b) Fe 2p and (c) Ni₂P@Fe₂P after LSV test. Table S1: Comparison of OER performances between Ni₂P@Fe₂P electrode and recently reported electrocatalysts in alkaline solution. References [28–43] is cited in the Supplementary Materials.

Author Contributions: Conceptualization, H.S., J.L. (Jingjing Li) and G.S.; methodology, G.S. and A.A.M.; software, A.A.M.; validation, R.Y., Y.F., S.Z. and J.L. (Juan Luo); formal analysis, R.Y. and Y.F.; investigation, S.Z.; resources, J.L. (Juan Luo); data curation, H.S. and J.L. (Jingjing Li); writing—original draft preparation, H.S., J.L. (Jingjing Li) and G.S.; writing—review and editing, W.S.; visualization, Z.W. and J.L. (Juan Luo); supervision, W.S.; project administration, W.S.; funding acquisition, W.S. All authors have read and agreed to the published version of the manuscript.

Funding: This work was supported by the National Natural Science Foundation of China (22075249, 51802281) and the Zhejiang Provincial Natural Science Foundation (LY21B010006).

Data Availability Statement: The data that support the findings of this study are available from the corresponding authors upon reasonable request.

Conflicts of Interest: There are no conflicts of interest to declare.

References

- Guan, J.; Shao, L.; Yu, L.; Wang, S.; Shi, X.; Cai, J.; Sun, Z. Two-Dimensional Mg_{0.2}V₂O₅·nH₂O Nanobelts Derived from V₄C₃ MXenes for Highly Stable Aqueous Zinc Ion Batteries. *Chem. Eng. J.* **2022**, *443*, 136502. [\[CrossRef\]](#)
- Li, Y.; Chen, J.; Cai, P.; Wen, Z. An Electrochemically Neutralized Energy-Assisted Low-Cost Acid-Alkaline Electrolyzer for Energy-Saving Electrolysis Hydrogen Generation. *J. Mater. Chem. A* **2018**, *6*, 4948–4954. [\[CrossRef\]](#)
- Liu, P.; Liu, W.; Huang, Y.; Li, P.; Yan, J.; Liu, K. Mesoporous Hollow Carbon Spheres Boosted, Integrated High Performance Aqueous Zn-Ion Energy Storage. *Energy Storage Mater.* **2020**, *25*, 858–865. [\[CrossRef\]](#)
- Wang, Z.; Zhou, Q.; Zhu, Y.; Du, Y.; Yang, W.; Chen, Y.; Li, Y.; Wang, S. NiFeMn-Layered Double Hydroxides Linked by Graphene as High-Performance Electrocatalysts for Oxygen Evolution Reaction. *Nanomaterials* **2022**, *12*, 2200. [\[CrossRef\]](#) [\[PubMed\]](#)
- Kim, J.; Heo, J.N.; Do, J.Y.; Chava, R.K.; Kang, M. Electrochemical Synergies of Heterostructured Fe₂O₃-MnO Catalyst for Oxygen Evolution Reaction in Alkaline Water Splitting. *Nanomaterials* **2019**, *9*, 1486. [\[CrossRef\]](#) [\[PubMed\]](#)
- Tian, X.; Yi, P.; Sun, J.; Li, C.; Liu, R.; Sun, J.-K. The Scalable Solid-State Synthesis of a Ni₅P₄/Ni₂P-FeNi Alloy Encapsulated into a Hierarchical Porous Carbon Framework for Efficient Oxygen Evolution Reactions. *Nanomaterials* **2022**, *12*, 1848. [\[CrossRef\]](#)
- Shang, X.; Chen, W.; Jiang, Z.-J.; Song, C.; Jiang, Z. In Situ Growth of SeOx Films on the Surface of Ni-Fe-Selenide Nanosheets as Highly Active and Stable Electrocatalysts for the Oxygen Evolution Reaction. *Mater. Adv.* **2022**, *3*, 2546–2557. [\[CrossRef\]](#)
- Jeon, J.; Park, K.R.; Kim, K.M.; Ko, D.; Han, H.; Oh, N.; Yeo, S.; Ahn, C.; Mhin, S. CoFeS₂@CoS₂ Nanocubes Entangled with CNT for Efficient Bifunctional Performance for Oxygen Evolution and Oxygen Reduction Reactions. *Nanomaterials* **2022**, *12*, 983. [\[CrossRef\]](#)
- Liu, D.; Ai, H.; Li, J.; Fang, M.; Chen, M.; Liu, D.; Du, X.; Zhou, P.; Li, F.; Lo, K.H.; et al. Surface Reconstruction and Phase Transition on Vanadium–Cobalt–Iron Trimetal Nitrides to Form Active Oxyhydroxide for Enhanced Electrocatalytic Water Oxidation. *Adv. Energy Mater.* **2020**, *10*, 2002464. [\[CrossRef\]](#)
- Li, Z.; Dou, X.; Zhao, Y.; Wu, C. Enhanced Oxygen Evolution Reaction of Metallic Nickel Phosphide Nanosheets by Surface Modification. *Inorg. Chem. Front.* **2016**, *3*, 1021–1027. [\[CrossRef\]](#)
- Wang, M.; Lin, M.; Li, J.; Huang, L.; Zhuang, Z.; Lin, C.; Zhou, L.; Mai, L. Metal–Organic Framework Derived Carbon-Confined Ni₂P Nanocrystals Supported on Graphene for an Efficient Oxygen Evolution Reaction. *Chem. Commun.* **2017**, *53*, 8372–8375. [\[CrossRef\]](#)
- Cheng, X.; Pan, Z.; Lei, C.; Jin, Y.; Yang, B.; Li, Z.; Zhang, X.; Lei, L.; Yuan, C.; Hou, Y. A Strongly Coupled 3D Ternary Fe₂O₃@Ni₂P/Ni(PO₃)₂ Hybrid for Enhanced Electrocatalytic Oxygen Evolution at Ultra-High Current Densities. *J. Mater. Chem. A* **2019**, *7*, 965–971. [\[CrossRef\]](#)
- Li, Y.; Wu, Y.; Hao, H.; Yuan, M.; Lv, Z.; Xu, L.; Wei, B. In Situ Unraveling Surface Reconstruction of Ni₅P₄@FeP Nanosheet Array for Superior Alkaline Oxygen Evolution Reaction. *Appl. Catal. B Environ.* **2022**, *305*, 121033. [\[CrossRef\]](#)
- Battiatto, S.; Urso, M.; Cosentino, S.; Pellegrino, A.L.; Mirabella, S.; Terrasi, A. Optimization of Oxygen Evolution Reaction with Electroless Deposited Ni–P Catalytic Nanocoating. *Nanomaterials* **2021**, *11*, 3010. [\[CrossRef\]](#)

15. Wang, J.; Niu, Y.; Teng, X.; Gong, S.; Huang, J.; Xu, M.; Chen, Z. Construction of Three-Dimensionally Ordered Macroporous Bimetal Phosphides as Bifunctional Electrocatalysts for Highly Efficient Water Splitting. *J. Mater. Chem. A* **2020**, *8*, 24572–24578. [\[CrossRef\]](#)
16. Costa, J.D.; Lado, J.L.; Carbó-Argibay, E.; Paz, E.; Gallo, J.; Cerqueira, M.F.; Rodríguez-Abreu, C.; Kovnir, K.; Kolen'ko, Y.V. Electrocatalytic Performance and Stability of Nanostructured Fe–Ni Pyrite-Type Diphosphide Catalyst Supported on Carbon Paper. *J. Phys. Chem. C* **2016**, *120*, 16537–16544. [\[CrossRef\]](#)
17. Lu, X.; Zhao, C. Electrodeposition of Hierarchically Structured Three-Dimensional Nickel–Iron Electrodes for Efficient Oxygen Evolution at High Current Densities. *Nat. Commun.* **2015**, *6*, 6616. [\[CrossRef\]](#)
18. Yu, Z.; Li, Y.; Martin-Diaconescu, V.; Simonelli, L.; Ruiz Esquius, J.; Amorim, I.; Araujo, A.; Meng, L.; Faria, J.L.; Liu, L. Highly Efficient and Stable Saline Water Electrolysis Enabled by Self-Supported Nickel-Iron Phosphosulfide Nanotubes with Heterointerfaces and Under-Coordinated Metal Active Sites. *Adv. Funct. Mater.* **2022**, 2206138. [\[CrossRef\]](#)
19. Yu, X.; Chen, W.; Cai, J.; Lu, X.; Sun, Z. Oxygen Vacancy-Rich MnO Nanoflakes/N-Doped Carbon Nanotubes Modified Separator Enabling Chemisorption and Catalytic Conversion of Polysulfides for Li-S Batteries. *J. Colloid Interface Sci.* **2022**, *610*, 407–417. [\[CrossRef\]](#)
20. Sun, J.; Xue, H.; Guo, N.; Song, T.; Hao, Y.; Sun, J.; Zhang, J.; Wang, Q. Synergetic Metal Defect and Surface Chemical Reconstruction into NiCo₂S₄/ZnS Heterojunction to Achieve Outstanding Oxygen Evolution Performance. *Angew. Chem. Int. Ed.* **2021**, *60*, 19435–19441. [\[CrossRef\]](#)
21. Wu, T.; Song, E.; Zhang, S.; Luo, M.; Zhao, C.; Zhao, W.; Liu, J.; Huang, F. Engineering Metallic Heterostructure Based on Ni₃N and 2M-MoS₂ for Alkaline Water Electrolysis with Industry-Compatible Current Density and Stability. *Adv. Mater.* **2022**, *34*, 2108505. [\[CrossRef\]](#) [\[PubMed\]](#)
22. Xia, J.; Zhao, H.; Huang, B.; Xu, L.; Luo, M.; Wang, J.; Luo, F.; Du, Y.; Yan, C.-H. Efficient Optimization of Electron/Oxygen Pathway by Constructing Ceria/Hydroxide Interface for Highly Active Oxygen Evolution Reaction. *Adv. Funct. Mater.* **2020**, *30*, 1908367. [\[CrossRef\]](#)
23. Chen, M.; Li, H.; Wu, C.; Liang, Y.; Qi, J.; Li, J.; Shanguan, E.; Zhang, W.; Cao, R. Interfacial Engineering of Heterostructured Co(OH)₂/NiP_x Nanosheets for Enhanced Oxygen Evolution Reaction. *Adv. Funct. Mater.* **2022**, 2206407. [\[CrossRef\]](#)
24. Ni, S.; Qu, H.; Xu, Z.; Zhu, X.; Xing, H.; Wang, L.; Yu, J.; Liu, H.; Chen, C.; Yang, L. Interfacial Engineering of the NiSe₂/FeSe₂ p-p Heterojunction for Promoting Oxygen Evolution Reaction and Electrocatalytic Urea Oxidation. *Appl. Catal. B Environ.* **2021**, *299*, 120638. [\[CrossRef\]](#)
25. Dutta, S.; Indra, A.; Feng, Y.; Song, T.; Paik, U. Self-Supported Nickel Iron Layered Double Hydroxide-Nickel Selenide Electrocatalyst for Superior Water Splitting Activity. *ACS Appl. Mater. Interfaces* **2017**, *9*, 33766–33774. [\[CrossRef\]](#) [\[PubMed\]](#)
26. Bernasconi, R.; Khalil, M.I.; Cakmakci, D.S.; Bektas, Y.; Nobili, L.; Magagnin, L.; Lenardi, C. Electrocatalytic Layers for Hydrogen Evolution Reaction Based on Nickel Phosphides: Cost-Effective Fabrication and XPS Characterization. *J. Mater. Sci.* **2022**, *57*, 9370–9388. [\[CrossRef\]](#)
27. Wan, K.; Luo, J.; Zhou, C.; Zhang, T.; Arbiol, J.; Lu, X.; Mao, B.; Zhang, X.; Fransae, J. Hierarchical Porous Ni₃S₄ with Enriched High-Valence Ni Sites as a Robust Electrocatalyst for Efficient Oxygen Evolution Reaction. *Adv. Funct. Mater.* **2019**, *29*, 1900315. [\[CrossRef\]](#)
28. Song, H.; Li, J.; Sheng, G.; Zhang, Y.; Mohamad, A.A.; Luo, J.; Zhong, Z.; Shao, W. Construction of Core–Shell CoMoO₄@γ-FeOOH Nanosheets for Efficient Oxygen Evolution Reaction. *Nanomaterials* **2022**, *12*, 2215. [\[CrossRef\]](#)
29. Li, X.; Liu, C.; Fang, Z.; Xu, L.; Lu, C.; Hou, W. Ultrafast Room-Temperature Synthesis of Self-Supported NiFe-Layered Double Hydroxide as Large-Current-Density Oxygen Evolution Electrocatalyst. *Small* **2022**, *18*, 2104354. [\[CrossRef\]](#)
30. Cai, Z.; Bu, X.; Wang, P.; Su, W.; Wei, R.; Ho, J.C.; Yang, J.; Wang, X. Simple and Cost Effective Fabrication of 3D Porous Core–Shell Ni Nanochains@NiFe Layered Double Hydroxide Nanosheet Bifunctional Electrocatalysts for Overall Water Splitting. *J. Mater. Chem. A* **2019**, *7*, 21722–21729. [\[CrossRef\]](#)
31. Zhang, P.; Li, L.; Nordlund, D.; Chen, H.; Fan, L.; Zhang, B.; Sheng, X.; Daniel, Q.; Sun, L. Dendritic Core-Shell Nickel-Iron-Copper Metal/Metal Oxide Electrode for Efficient Electrocatalytic Water Oxidation. *Nat. Commun.* **2018**, *9*, 381. [\[CrossRef\]](#)
32. Senthil, R.A.; Pan, J.; Yang, X.; Sun, Y. Nickel Foam-Supported NiFe Layered Double Hydroxides Nanoflakes Array as a Greatly Enhanced Electrocatalyst for Oxygen Evolution Reaction. *Int. J. Hydrogen Energy* **2018**, *43*, 21824–21834. [\[CrossRef\]](#)
33. Liu, X.; Gong, M.; Xiao, D.; Deng, S.; Liang, J.; Zhao, T.; Lu, Y.; Shen, T.; Zhang, J.; Wang, D. Turning Waste into Treasure: Regulating the Oxygen Corrosion on Fe Foam for Efficient Electrocatalysis. *Small* **2020**, *16*, 2000663. [\[CrossRef\]](#)
34. Che, Q.; Li, Q.; Chen, X.; Tan, Y.; Xu, X. Assembling Amorphous (Fe–Ni)Co–OH/Ni₃S₂ Nanohybrids with S-Vacancy and Interfacial Effects as an Ultra-Highly Efficient Electrocatalyst: Inner Investigation of Mechanism for Alkaline Water-to-Hydrogen/Oxygen Conversion. *Appl. Catal. B Environ.* **2020**, *263*, 118338. [\[CrossRef\]](#)
35. Zhu, G.; Li, X.; Liu, Y.; Mao, Y.; Liang, Z.; Ji, Z.; Shen, X.; Sun, J.; Cheng, X.; Mao, J. Scalable Surface Engineering of Commercial Metal Foams for Defect-Rich Hydroxides towards Improved Oxygen Evolution. *J. Mater. Chem. A* **2020**, *8*, 12603–12612. [\[CrossRef\]](#)
36. Jin, Y.; Huang, S.; Yue, X.; Shu, C.; Shen, P.K. Highly Stable and Efficient Non-Precious Metal Electrocatalysts of Mo-Doped NiOOH Nanosheets for Oxygen Evolution Reaction. *Int. J. Hydrogen Energy* **2018**, *43*, 12140–12145. [\[CrossRef\]](#)
37. Qiu, C.; He, S.; Wang, Y.; Wang, Q.; Zhao, C. Interfacial Engineering FeOOH/CoO Nanoneedle Array for Efficient Overall Water Splitting Driven by Solar Energy. *Chem.–Eur. J.* **2020**, *26*, 4120–4127. [\[CrossRef\]](#)

38. Liu, T.; Diao, P. Nickel Foam Supported Cr-Doped NiCo₂O₄/FeOOH Nanoneedle Arrays as a High-Performance Bifunctional Electrocatalyst for Overall Water Splitting. *Nano Res.* **2020**, *13*, 3299–3309. [[CrossRef](#)]
39. Yu, L.; Wu, L.; McElhenny, B.; Song, S.; Luo, D.; Zhang, F.; Yu, Y.; Chen, S.; Ren, Z. Ultrafast Room-Temperature Synthesis of Porous S-Doped Ni/Fe (Oxy)Hydroxide Electrodes for Oxygen Evolution Catalysis in Seawater Splitting. *Energy Environ. Sci.* **2020**, *13*, 3439–3446. [[CrossRef](#)]
40. Chi, J.; Yu, H.; Jiang, G.; Jia, J.; Qin, B.; Yi, B.; Shao, Z. Construction of Orderly Hierarchical FeOOH/NiFe Layered Double Hydroxides Supported on Cobaltous Carbonate Hydroxide Nanowire Arrays for a Highly Efficient Oxygen Evolution Reaction. *J. Mater. Chem. A* **2018**, *6*, 3397–3401. [[CrossRef](#)]
41. Zhang, X.; Yi, H.; Jin, M.; Lian, Q.; Huang, Y.; Ai, Z.; Huang, R.; Zuo, Z.; Tang, C.; Amini, A.; et al. In Situ Reconstructed Zn Doped Fe_xNi_(1-x) OOH Catalyst for Efficient and Ultrastable Oxygen Evolution Reaction at High Current Densities. *Small* **2022**, 2203710. [[CrossRef](#)]
42. Feng, J.-X.; Ye, S.-H.; Xu, H.; Tong, Y.-X.; Li, G.-R. Design and Synthesis of FeOOH/CeO₂ Heterolayered Nanotube Electrocatalysts for the Oxygen Evolution Reaction. *Adv. Mater.* **2016**, *28*, 4698–4703. [[CrossRef](#)]
43. Liang, J.; Gao, X.; Guo, B.; Ding, Y.; Yan, J.; Guo, Z.; Tse, E.C.M.; Liu, J. Ferrocene-Based Metal–Organic Framework Nanosheets as a Robust Oxygen Evolution Catalyst. *Angew. Chem. Int. Ed.* **2021**, *60*, 12770–12774. [[CrossRef](#)]
44. Liu, Y.; Chen, Y.; Tian, Y.; Sakthivel, T.; Liu, H.; Guo, S.; Zeng, H.; Dai, Z. Synergizing Hydrogen Spillover and Deprotonation by the Internal Polarization Field in a MoS₂/NiPS₃ Vertical Heterostructure for Boosted Water Electrolysis. *Adv. Mater.* **2022**, 2203615. [[CrossRef](#)]
45. Nai, J.; Xu, X.; Xie, Q.; Lu, G.; Wang, Y.; Luan, D.; Tao, X.; Lou, X.W. Construction of Ni(CN)₂/NiSe₂ Heterostructures by Stepwise Topochemical Pathways for Efficient Electrocatalytic Oxygen Evolution. *Adv. Mater.* **2022**, *34*, 2104405. [[CrossRef](#)]
46. Li, N.; Bediako, D.K.; Hadt, R.G.; Hayes, D.; Kempa, T.J.; von Cube, F.; Bell, D.C.; Chen, L.X.; Nocera, D.G. Influence of Iron Doping on Tetravalent Nickel Content in Catalytic Oxygen Evolving Films. *Proc. Natl. Acad. Sci. USA* **2017**, *114*, 1486–1491. [[CrossRef](#)]
47. Han, M.; Wang, N.; Zhang, B.; Xia, Y.; Li, J.; Han, J.; Yao, K.; Gao, C.; He, C.; Liu, Y.; et al. High-Valent Nickel Promoted by Atomically Embedded Copper for Efficient Water Oxidation. *ACS Catal.* **2020**, *10*, 9725–9734. [[CrossRef](#)]
48. Lee, W.H.; Han, M.H.; Ko, Y.-J.; Min, B.K.; Chae, K.H.; Oh, H.-S. Electrode Reconstruction Strategy for Oxygen Evolution Reaction: Maintaining Fe-CoOOH Phase with Intermediate-Spin State during Electrolysis. *Nat. Commun.* **2022**, *13*, 605. [[CrossRef](#)]
49. Xu, Q.; Jiang, H.; Duan, X.; Jiang, Z.; Hu, Y.; Boettcher, S.W.; Zhang, W.; Guo, S.; Li, C. Fluorination-Enabled Reconstruction of NiFe Electrocatalysts for Efficient Water Oxidation. *Nano Lett.* **2021**, *21*, 492–499. [[CrossRef](#)]
50. Wang, Y.; Zhu, Y.; Zhao, S.; She, S.; Zhang, F.; Chen, Y.; Williams, T.; Gengenbach, T.; Zu, L.; Mao, H.; et al. Anion Etching for Accessing Rapid and Deep Self-Reconstruction of Precatalysts for Water Oxidation. *Matter* **2020**, *3*, 2124–2137. [[CrossRef](#)]